JOURNAL OF COMPUTATIONAL PHYSICS 117, 318–331 (1995)

The Second-Order Projection Method for the Backward-Facing Step Flow

JINGYI ZHU*

Department of Mathematics, University of Utah, Salt Lake City, Utah 84112

Received December 7, 1992; revised April 25, 1994

In an effort to demonstrate the validity of the second-order projection method for incompressible and viscous flows inside irregular domains, we use the method to study the flow in the two-dimensional channel with a backward-facing step. The emphasis of our study is on the flow separation and reattachment phenomena. Calculations are performed over a wide range of Reynolds numbers, including the laminar, transitional, and turbulent regimes defined by experiments. In the laminar regime, we find excellent agreement with experiments in terms of the dependence of the reattachment length on the Reynolds number and streamwise velocity profiles. For Reynolds numbers beyond the laminar regime, where there are no two-dimensional experimental data available for comparison, we find characteristic flow structures similar to those observed in three-dimensional experiments. For such physically unstable flows, we are able to show certain numerical convergence in the statistical behavior of the solution. Comparison with the random vortex method is also made and similar flow behavior is found in both solutions. © 1995 Academic Press, Inc.

1. INTRODUCTION

The analysis of incompressible and viscous flow structures with high Reynolds numbers inside irregular domains is one of the fundamental subjects in fluid dynamics. The interests and difficulties arise from the fact that flow separation and subsequent reattachment usually occur, which would cause the Prandtl boundary layer approximation to be invalid and would result in a complex structure of vortex dynamics. It is well known and easy to realize that the phenomenon is extremely important in engineering designs (for instance, the design of a combustion chamber). Among such problems, the flow in a long channel with a backward-facing step stands out as a widely accepted model problem. This is due to the fact that the geometry in this problem is relatively simple, but it contains all the essential features of the type of problems we mentioned above. Also, experimental results indicate that this flow has three distinct flow regimes (laminar, transitional, and turbulent) that are well defined by the Reynolds number. This makes it very well suited to study a numerical method for its correct dependence on the Reynolds number. Over the years, there has been a great amount of work devoted to this problem from both experimental and numerical approaches. However, due to the difficulties associated with flows with high Reynolds numbers, most early computational works dealt with the laminar regime only. A summary of these numerical results for the steady case can be found in [15]. The random vortex method was first applied to this flow at high Reynolds numbers by Ashurst [2] to study the turbulent shear stress and by Ghoniem, Chorin, and Oppenheim [10] in a combustion problem. More detailed and careful studies of the step problem by the random vortex method were carried out by Ghoniem and Sethian [11, 16]. In these works flows are computed at Reynolds numbers up to 5000, and different flow structures corresponding to different regimes similar to those in experiments were observed. In this regard, it was a breakthrough in numerical simulations for this problem. For accuracy of the random vortex method in the step problem, careful calculations were performed by Ghoniem and Cagnon [12] in the laminar regime at moderate Reynolds numbers. In this work, we provide a finite difference approach as an alternative to the vortex method approach. The accuracy of the method is studied quantitatively in the laminar regime and flow structures at Reynolds numbers beyond the laminar regime are also considered. We compare our numerical results with those in [16, 12] to validate both numerical approaches. For comparisons with experiments, we refer mostly to the works of Armaly, Durst, Pereira, and Schonuay [1] and Denham and Patrick [8].

Here, we apply a second-order projection method developed by Bell, Colella, and Glaz [3], combined with our choice of a outflow boundary condition, to solve the step channel problem. This finite difference method incorporates a Godunov type upwind scheme in the advection term and a Galerkin approximation in the projection step. As a result, the method has an improved performance concerning the numerical viscosity, which enables us to compute flows beyond the laminar regime.

The paper is divided into two parts. In the first part, we describe the flow problem carefully and review the second-order projection method briefly. We explain the definition of

---

* This work was supported in part by the Applied Mathematical Sciences subprogram of the Office of Energy under Contract DE-AC03-76SF00098.

0021-9991/95 $6.00
Copyright © 1995 by Academic Press, Inc.
All rights of reproduction in any form reserved.

the discrete incompressibility condition and our choice of the outflow boundary condition in details. In the second part, we start with a careful comparison of our numerical results with experimental data in the laminar regime, emphasizing the reattachment length and streamwise velocity profiles. In the transitional and turbulent regimes, it is well known that no experiment is exactly two-dimensional. Therefore no exact comparison is possible in these two regimes. Nevertheless we have some qualitative agreements in the characteristics of the flow. As a numerical simulation to the two-dimensional Navier–Stokes equations in an unstable flow regime, we are able to present some numerical convergence in the velocity fluctuations.

2. THE FLOW PROBLEM AND THE NUMERICAL ALGORITHM

We consider a two-dimensional, incompressible, and viscous flow in a channel with a backward-facing step. The governing equations are the Navier–Stokes equations,

$$\mathbf{u}_t + \mathbf{u} \cdot \nabla \mathbf{u} = -\nabla p + \frac{1}{\mathrm{Re}} \nabla^2 \mathbf{u}, \tag{1}$$

$$\nabla \cdot \mathbf{u} = 0, \tag{2}$$

where $\mathbf{u} = (u, v)$ is the velocity of the fluid, normalized with respect to the averaged velocity U at the inlet; the length variables are normalized with respect to the step height H; t is the time normalized with respect to H/U; and p is the pressure normalized with respect to ρU^2. Re is the Reynolds number of the flow and we use $\mathrm{Re} = HU/\nu$, where ν is the kinematic viscosity. This definition of Re agrees with the definitions in [16, 8]. When it is compared to the definition of Re in [1], there is a difference of a factor of 2. We will take into account this difference when we compare the results. Other geometric parameters in this problem are the channel height D, the inlet length W_I and the outlet length W_E. The geometry of the step channel is characterized by the expansion ratio $D/(D - H)$. An example is shown in Fig. 1a with $H = 1$ and $D = 2$.

The boundary conditions are imposed on $\mathbf{u}$, but not on p. For the step channel geometry with boundaries $\partial\Omega_1$, $\partial\Omega_2$, and $\partial\Omega_3$ shown in Fig. 1a, we pose the boundary condition

$$\mathbf{u} = \begin{cases} 0, & \text{on } \partial\Omega_1, \\ (f(y), 0), & \text{on } \partial\Omega_2, \end{cases} \tag{3}$$

where the inlet x-velocity profile $f(y)$ is a given function.

The choices of channel lengths W_I and W_E affect the flow development and they are important factors when we compare our results with others. At the channel exit ($x = W_\mathrm{E}$) we need to impose an outflow condition. The effects of the outflow condition on flow properties that we are interested are expected to diminish if the channel is sufficiently long. At the inlet ($x = -W_\mathrm{I}$) we need to prescribe some x-velocity profile $f(y)$. A sufficient inlet length W_I is also required to develop the flow. In the laminar regime the flow is expected to be developed into a Poiseuille profile downstream before the step. For most experiments, certain apparatus are used before the channel inlet to make sure that the flow is fully developed. In our calculations this can be achieved by increasing the length W_I. Several choices for the inlet profile f are possible. For example, we can impose a Poiseuille profile. However, there is a concern that when the Reynolds number is high enough, the flow becomes physically unstable. Then imposing a stable Poiseuille profile will be inappropriate. In [16, 12] a uniform inlet profile $f(y) = 1$ was chosen for reasons concerning the creation of vorticity and the instability concern explained above. Here we choose this profile for the same reasons, so we can compare the numerical results. As we mentioned above, the disadvantage can be compensated to a certain extent by increasing W_I and we will study this effect in our numerical calculations.

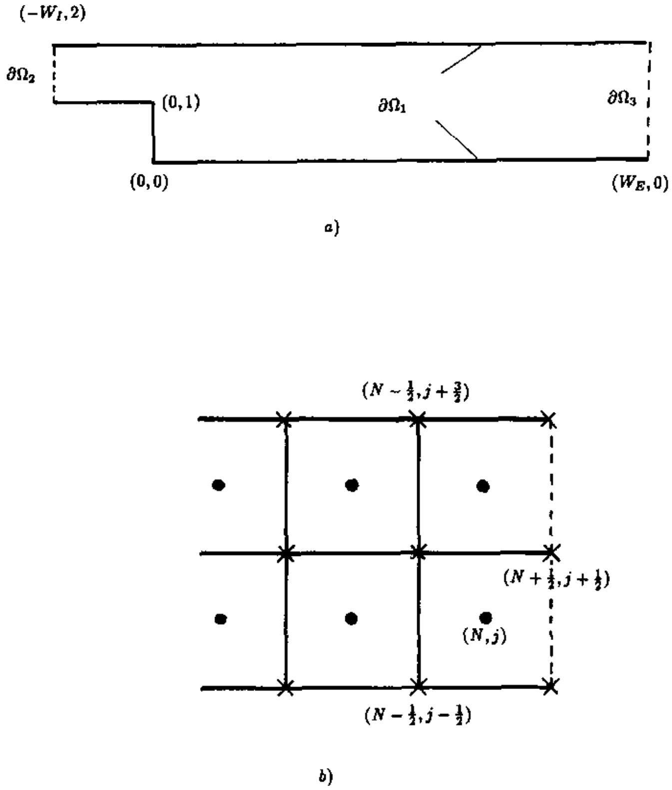

FIG. 1. (a) Geometry of the computation domain. (b) A stencil on the outflow boundary.

The nature of the flow poses a serious challenge to any numerical method due to the fact that the flow is physically unstable in the regimes in which we are interested. It is also well known that finite difference methods generate a certain amount of numerical viscosity. When the Reynolds number goes beyond a certain value, the numerical viscosity will surpass the physical viscosity, thus causing an effective viscosity which makes the calculations meaningless. Therefore, to study the flow behavior in Reynolds number ranges beyond the laminar regime, numerical methods with minimum numerical viscosity are essential to the success. The random vortex method, introduced by Chorin, is free of the type of numerical viscosity from spatial discretization and has been very successful in dealing with high Reynolds number flows. In [16, 11] it was used to obtain numerical solutions for very high Reynolds numbers which had not been numerically obtained before. However, the random walks used in the random vortex method to simulate the viscosity introduce certain numerical noise into calculations, and it is not so clear if they always represent the physical noise in experiments. This happens especially when the number of vortex elements used is not large enough and the flow is not fully turbulent. Also, the random vortex method generates vorticity from boundaries and the number of vortex elements grows in time, unless some deleting mechanism is used. Therefore, a finite difference calculation with high-order accuracy and low numerical viscosity would be important for us to better understand this particular flow.

The second-order projection method, developed by Bell, Colella, and Glaz [3], emphasizes the following two aspects: (1) the requirement of satisfying a discrete divergence-free condition at every time step, and (2) a second-order approximation of the advection term with a state-of-the-art upwind technique originally introduced for compressible flows by Colella [7]. Here we briefly summarize the algorithm.

First, we partition the domain into a collection of cells with velocity $\mathbf{u}_{i,j}$ defined at cell centers and pressure $p_{i+1/2,j+1/2}$, defined at cell corners. The Navier–Stokes equations are discretized at cell centers. Assume that at the nth time step, $\mathbf{u}^n$ and $p^{n-1/2}$ are given. We want to solve $\mathbf{u}^{n+1}$ and $p^{n+1/2}$ in the Crank–Nicholson approximation

$$\frac{\mathbf{u}^{n+1}-\mathbf{u}^n}{\Delta t}+(\mathbf{u}\cdot\nabla\mathbf{u})^{n+1/2}=-\nabla p^{n+1/2}+\frac{1}{2\mathrm{Re}}\nabla^2(\mathbf{u}^{n+1}+\mathbf{u}^n) \tag{4}$$

with

$$\nabla\cdot\mathbf{u}^{n+1}=0. \tag{5}$$

The essence of the method is to solve Eqs. (4) and (5) in two steps. First, by ignoring the divergence-free condition (5), we solve for an intermediate velocity field $\mathbf{u}^{n+1,*}$ in the equation

$$\frac{\mathbf{u}^{n+1,*}-\mathbf{u}^n}{\Delta t}+(\mathbf{u}\cdot\nabla\mathbf{u})^{n+1/2}=-\nabla p^{n+1/2,*}+\frac{1}{2\mathrm{Re}}\nabla^2(\mathbf{u}^{n+1,*}+\mathbf{u}^n), \tag{6}$$

where $p^{n+1/2,*}$ is a reasonable approximation to $p^{n+1/2}$. In our calculations, we use the previous time step solution $p^{n-1/2}$ as a first guess. The sophisticated algorithm to calculate explicitly the nonlinear term $(\mathbf{u}\cdot\nabla\mathbf{u})^{n+1/2}$ is a major part of the method and the details can be found in [3, 7]. It should be mentioned here that the explicit calculation of the nonlinear term requires a CFL condition. Equation (6) is a heat equation with a given forcing term. We can use the conjugate gradient method, without any preconditioning, to solve the discretized system of this equation. The boundary conditions for $\mathbf{u}^{n+1,*}$ are the same as $\mathbf{u}^{n+1}$, except that at the flow exit we impose

$$\frac{\partial}{\partial x}\mathbf{u}^{n+1,*}=0. \tag{7}$$

The second step is to project $\mathbf{u}^{n+1,*}$ onto the discrete divergence-free velocity subspace and update the pressure as

$$\mathbf{u}^{n+1,*}=\mathbf{u}^{n+1}+\Delta t(\nabla p^{n+1/2}-\nabla p^{n+1/2,*}), \tag{8}$$

with $\mathbf{u}^{n+1}$ satisfying Eq. (5).

The projection method was introduced by Chorin [5, 6]. The concept was motivated by the Hodge decomposition, which states that any vector field $\mathbf{v}$ in a bounded domain Ω can be uniquely decomposed into a divergence-free vector $\mathbf{u}$, whose normal component vanishes on the boundary, and the gradient of some scalar field ϕ. The orthogonality follows from the integration by parts procedure

$$\int_\Omega \mathbf{u}\cdot\nabla\phi\,d\mathbf{x}=-\int_\Omega \phi\nabla\cdot\mathbf{u}\,d\mathbf{x}+\int_{\partial\Omega}\phi\mathbf{u}\cdot\mathbf{n}\,dS. \tag{9}$$

The definition of numerical projection is based on a discrete version of Eq. (9). We choose some appropriate discrete operators G and D to approximate the gradient and the divergence operators so that

$$\langle\mathbf{u},G\phi\rangle_v=0, \tag{10}$$

for $\mathbf{u}$ that satisfies $D\mathbf{u}=0$ and the given boundary conditions, where $\langle\,,\rangle_v$ represents an inner product on a discrete space of vectors. The fact that we can choose the inner product according to D and G makes it possible to decompose the velocity space for boundary conditions other than the no-flux condition stated in the original Hodge decomposition. In the following we modify the inner product for the boundary conditions that we consider in this channel problem.

First, following the choice of [3], we define

$$(G\phi)_{i,j} = \begin{pmatrix} \dfrac{1}{2\Delta x}(\phi_{i+1/2,j+1/2} + \phi_{i+1/2,j-1/2} - \phi_{i-1/2,j+1/2} - \phi_{i-1/2,j-1/2}) \\ \dfrac{1}{2\Delta y}(\phi_{i+1/2,j+1/2} + \phi_{i-1/2,j+1/2} - \phi_{i+1/2,j-1/2} - \phi_{i-1/2,j-1/2}) \end{pmatrix}. \tag{11}$$

If the homogeneous Dirichlet boundary condition is imposed, the discrete divergence operator D is implicitly defined through the summation-by-parts procedure

$$\langle \mathbf{u}, G\phi\rangle_v = -\langle D\mathbf{u}, \phi\rangle_s, \tag{12}$$

where

$$\langle \mathbf{u}_1, \mathbf{u}_2\rangle_v = \sum_{i,j} (u_{1i,j}u_{2i,j} + v_{1i,j}v_{2i,j}), \tag{13}$$

for vectors $\mathbf{u}_1 = (u_1, v_1)$ and $\mathbf{u}_2 = (u_2, v_2)$, with summation over all cell centers, and

$$\langle \phi, \psi\rangle_s = \sum_{i,j} \phi_{i+1/2,j+1/2}\psi_{i+1/2,j+1/2}, \tag{14}$$

for scalars ϕ and ψ, with summation over all cell corners $(i + 1/2, j + 1/2)$.

Equation (12) establishes the orthogonality condition between the velocity subspace that satisfies conditions $D\mathbf{u} = 0$ and $\mathbf{u} = 0$ on the boundaries, and the subspace of $G\phi$. Actually we can find an explicit basis $\{\mathbf{u}^{i+1/2,j+1/2}\}$ for the first subspace, which comes from the discrete stream functions. Then $\mathbf{u}$ can be written as

$$\mathbf{u} = \sum_{i,j} \alpha_{i+1/2,j+1/2}\mathbf{u}^{i+1/2,j+1/2}, \tag{15}$$

with summation over all interior cell corners $(i + \frac12, j + \frac12)$.

To obtain $\mathbf{u}^{i+1/2,j+1/2}$, we consider the discrete stream function $\psi^{i+1/2,j+1/2}$, which is 1 at $(i + \frac12, j + \frac12)$ and zero at all other cell corners. Then

$$\mathbf{u}^{i+1/2,j+1/2} = G^{\perp}\psi^{i+1/2,j+1/2} \tag{16}$$

vanishes on the boundary if the cell corner $(i + \frac12, j + \frac12)$ is not on the boundary. They form a basis for the divergence-free velocity subspace that satisfies the homogeneous boundary condition (Stephens, Bell, Solomon, and Hackerman [17]). The projection of an arbitrary velocity field $\mathbf{v}$ onto this subspace is equivalent to solving for $\mathbf{u}$ in the system

$$\langle \mathbf{u}, \mathbf{u}^{i+1/2,j+1/2}\rangle_v = \langle \mathbf{v}, \mathbf{u}^{i+1/2,j+1/2}\rangle_v, \tag{17}$$

for all interior cell corners $(i + \frac12, j + \frac12)$.

Now let us consider the situation where an outflow boundary condition is imposed on one part of the boundary. We choose to use the natural boundary condition used by Bell and Marcus [4] as follows. The projection is still defined through Eq. (17), with some modifications to the basis for the discrete divergence-free velocity subspace. Since $\mathbf{u}$ in the subspace does not satisfy the Dirichlet boundary condition on the outflow exit, the basis for the discrete divergence-free velocity subspace should be expanded. This can be done by including the contributions from the discrete stream functions $\psi^{i+1/2,j+1/2}$ for the outflow boundary points, that is,

$$\mathbf{u} = \sum_{i,j} \alpha_{i+1/2,j+1/2}G^{\perp}\psi^{i+1/2,j+1/2} \tag{18}$$

for all interior cell corners *and* cell corners on the outflow boundary. Given the definitions of D and G, the inclusion of those contributions from the outflow boundary points in Eq. (18), in general, is not consistent with Eq. (12), unless certain boundary conditions are assumed at those boundary points.

Consider such a mesh point (N, j) on the outflow boundary shown in Fig. 1b; Eq. (17) gives

$$\alpha_{N+1/2,j+1/2} - \tfrac12(\alpha_{N-1/2,j+3/2} + \alpha_{N-1/2,j-1/2}) = \langle \mathbf{v}, \mathbf{u}^{N+1/2,j+1/2}\rangle_v = f_{N,j}, \tag{19}$$

where $\mathbf{v} = (v_1, v_2)$ and

$$f_{N,j} = \tfrac12(-v_{1N,j+1} - v_{2N,j+1} + v_{1N,j} - v_{2N,j}). \tag{20}$$

Comparing Eq. (19) with the corresponding equation for an interior point (i, j),

$$2\alpha_{i+1/2,j+1/2} - \tfrac12(\alpha_{i-1/2,j+3/2} + \alpha_{i-1/2,j-1/2} + \alpha_{i+3/2,j+3/2} + \alpha_{i+3/2,j-1/2}) = \langle \mathbf{v}, \mathbf{u}^{i+1/2,j+1/2}\rangle_v, \tag{21}$$

where

$$\langle \mathbf{v}, \mathbf{u}^{i+1/2,j+1/2}\rangle_v = \tfrac12(-v_{1i,j+1} - v_{2i,j+1} + v_{1i,j} - v_{2i,j} - v_{1i+1,j+1} + v_{2i+1,j+1} + v_{1i+1,j} + v_{2i+1,j}), \tag{22}$$

we can see that if Eq. (21) and Eq. (19) are consistent with each other, the continuous stream function must satisfy

$$\frac{\partial\psi}{\partial n} = -\mathbf{v}\cdot\tau, \tag{23}$$

where τ is the unit tangential vector along the outflow boundary. Since $\mathbf{u}\cdot\tau = -\partial\psi/\partial\mathbf{n}$, we conclude that

$$\mathbf{v}\cdot\tau = \mathbf{u}\cdot\tau \tag{24}$$

on the outflow boundary.

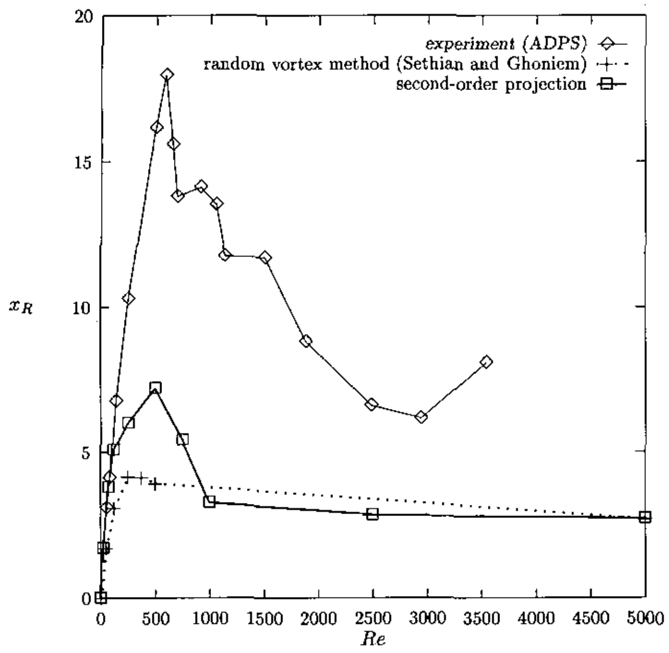

FIG. 2. The mean reattachment length x_R as a function of Re.

For the projection of the intermediate velocity $\mathbf{v}^{n+1}$, we have

$$\mathbf{v}^{n+1} = \mathbf{u}^{n+1} + \Delta t(\nabla p^{n+1/2} - \nabla p^{n-1/2}), \tag{25}$$

the conclusion in Eq. (24) implies that

$$\frac{\partial p}{\partial \tau}(t) = 0 \quad \text{on } \partial\Omega_3, t > 0. \tag{26}$$

The above argument shows that Eq. (12) is satisfied only if the pressure boundary condition (26) is assumed. It is reasonable to assume this boundary condition in our problem because there are no external forces applied near the outflow boundary (we ignore the gravity influence). However, for a nonzero external force $\mathbf{F}$, the pressure gradient is required to balance the external force so that

$$\frac{\partial p}{\partial \tau} = \mathbf{F} \cdot \tau \quad \text{on } \partial\Omega_3. \tag{27}$$

This can be achieved by adding a boundary term approximating $\int_{\partial\Omega_3} \mathbf{F} \cdot \tau \, dS$ to (17) (see [4] for details).

The inhomogeneous Dirichlet boundary condition on $\delta\Omega_1$ and $\partial\Omega_2$ can be easily incorporated by adding a known discrete incompressible velocity field satisfying the given Dirichlet boundary condition to the representation (18) (see [17]).

3. NUMERICAL RESULTS AND COMPARISONS WITH OTHERS

To compare with the experimental results [1, 8], we consider channels with two different expansion ratios: a ratio of 2 : 1 for comparisons with [1, 16] over a wide range of Reynolds numbers; and a ratio of 3 : 2 for a streamwise velocity profile comparison with [8, 12] in the laminar regime. Following the classification in [1], we studied the flow structures in three different Reynolds number ranges: the laminar (Re < 600), the transitional (600 < Re < 3300), and the turbulent (Re > 3300) regimes of this flow. We choose the step height $H = 1$, the channel length $W_E = 18$, and the channel height $D = 2$ for the expansion ratio 2 : 1, $D = 3$ for the expansion ratio 3 : 2. We use an uniform inlet profile $f(y) = 1$ at the channel inlet and we have varied the inlet length W_I to study its effect on the flow development. The grids we use are uniform with $\Delta x = \Delta y = h$ and we have studied the numerical solutions with $h = \frac{1}{32}$ and $\frac{1}{48}$. The flow is started impulsively at $t = 0$ and it is iterated 20 times to obtain a reasonable initial pressure field before continuing calculations for $t > 0$.

In [1], it was found that two-dimensional flows in the channel can only be generated for Re < 200 or Re > 3000. Due to this fact, it is not surprising that the definitions of these three regimes in two-dimensional computations are different. In the experiments these regimes are introduced to characterize the flow nature, and they are defined based on the behavior of the *mean* reattachment length x_R for its dependence on the Reynolds number. When the Reynolds number increases, the mean reat-

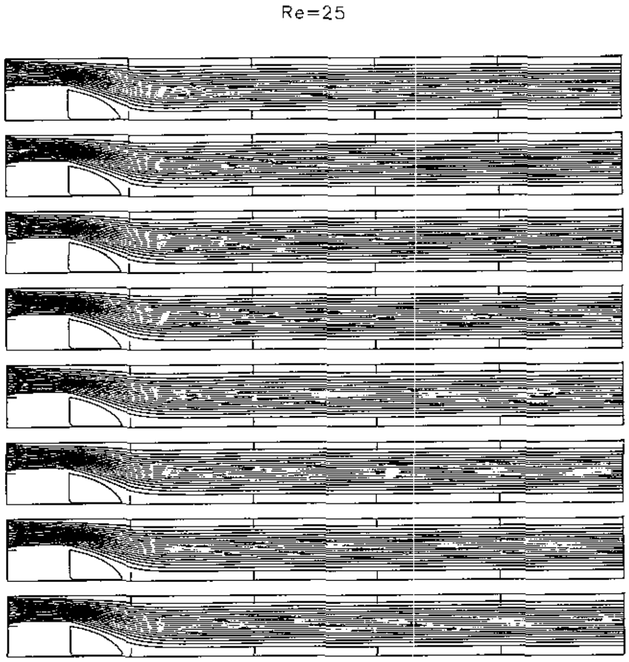

FIG. 3. Instantaneous streamline contours: Re = 25, $h = \frac{1}{32}$, and t = 5, 10, 15, 20, 25, 30, 35, 40.

TABLE I

Convergence to the Steady State

	$e(t)$						
Re	t = 5.	t = 10.	t = 15.	t = 20.	t = 25.	t = 30.	t = 35.
25.	1.23E-2	1.77E-3	2.47E-4	1.81E-5			
75.	1.22E-1	7.62E-2	4.41E-2	2.47E-2	1.32E-2	6.34E-3	2.24E-3
125.	1.97E-1	1.66E-1	1.23E-1	8.60E-2	5.63E-2	3.31E-2	1.42E-2
250.	2.91E-1	2.90E-1	2.61E-1	2.25E-1	1.76E-1	1.30E-1	6.66E-2

tachment length first increases, then it decreases, and finally it fluctuates along a constant. These critical Reynolds numbers, where the mean reattachment length changes its behavior, are used to define the laminar, transitional, and turbulent regimes.

In Fig. 2, we plot the dependence of the *mean* reattachment length on the Reynolds number for $25 \leq \mathrm{Re} \leq 5000$, from the results of our calculations, the random vortex method [16], and the corresponding experiments [1]. The expansion ratio in this case is 2 : 1. It is obvious that the phenomenon observed in three-dimensional experiments is also manifest in our two-dimensional calculations, although with different critical Reynolds numbers. Therefore, we can modify the definitions of the regimes in two-dimensional calculations accordingly.

Our procedure to calculate the reattachment length from a stream function $\psi(x, y)$ on the grid points is as follows. For each line $y = y_j$, $y_j > 0$, we use a linear interpolation to obtain the zeros x, where $\psi(x, y_j) = 0$. Then we connect all the zeros from different lines to obtain the zero curve. Finally we linearly extrapolate the zero curve to the wall and locate the reattachment point. For $\mathrm{Re} \leq 250$, we take the stream function at $t = 40$ to calculate x_R. For unsteady flows ($\mathrm{Re} > 250$) the stream function used is the averaged stream function over a time window [40, 78.75]. In these calculations, we used a 640×64 grid and an inlet channel length $W_I = 2$.

In the following, we discuss each regime separately. For each regime we will proceed with a brief description of the experimental results and then compare with our numerical results. For a more thorough summary of various experimental results, the readers are referred to [16].

3.1. *Laminar Regime*

In the laminar regime, the flow is characterized by a recirculation region, which starts from the separation at the step and

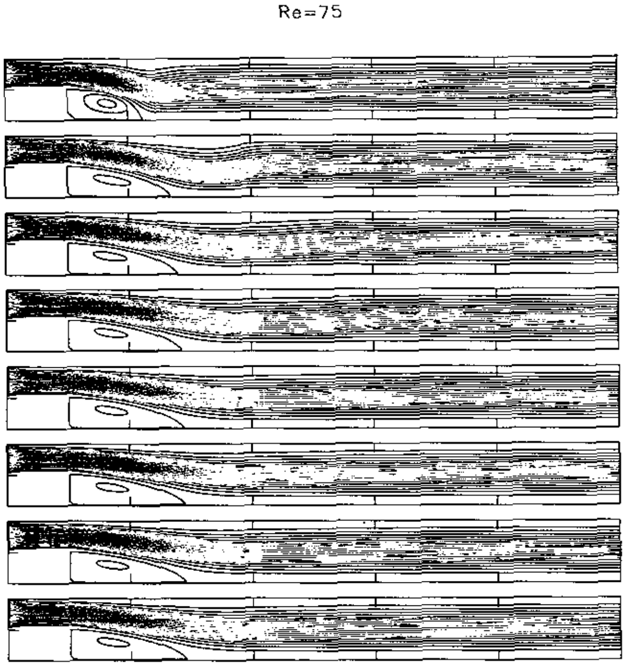

FIG. 4. Instantaneous streamline contours: Re = 75, $h = \frac{1}{32}$, and t = 5, 10, 15, 20, 25, 30, 35, 40.

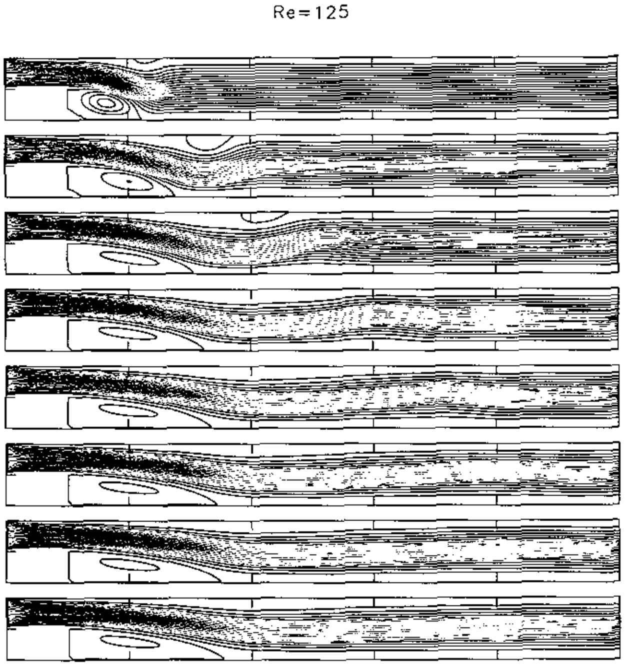

FIG. 5. Instantaneous streamline contours: Re = 125, $h = \frac{1}{32}$, and t = 5, 10, 15, 20, 25, 30, 35, 40.

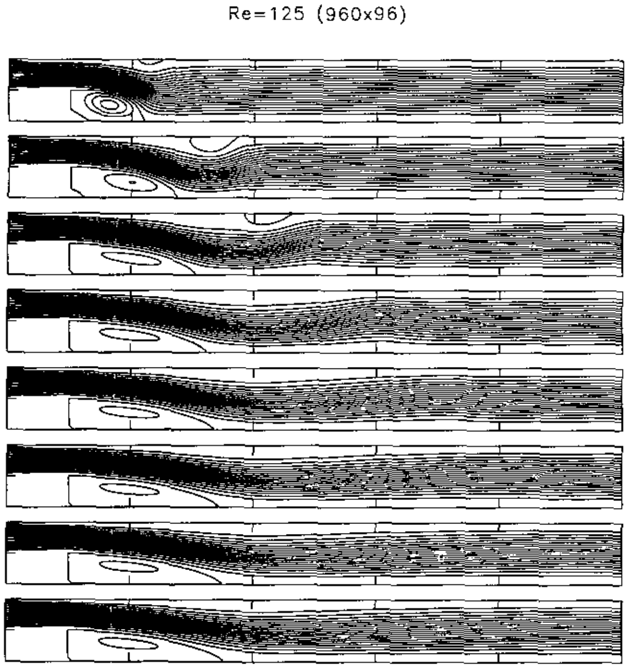

FIG. 6. Instantaneous streamline contours: Re = 125, $h = \frac{1}{48}$, and t = 5, 10, 15, 20, 25, 30, 35, 40.

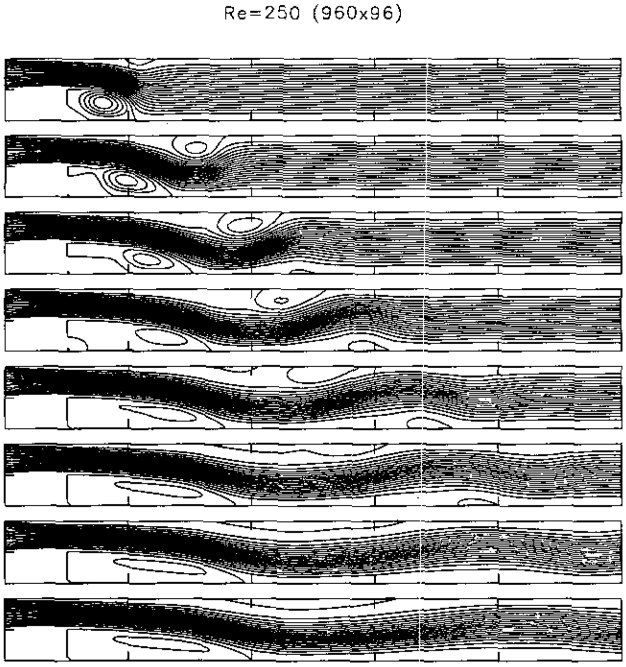

FIG. 8. Instantaneous streamline contours: Re = 250, $h = \frac{1}{48}$, and t = 5, 10, 15, 20, 25, 30, 35, 40.

ends at a reattachment point on the lower wall. The immediate interest is to study the dependence of the reattachment length x_R on the Reynolds number. In [1] it was reported that x_R increases with the Reynolds number in a nonlinear fashion, contrary to some predictions inferred from experiments with a similar geometry [13]. Various experiments also show that the flow is reasonably steady in the lower end of the regime, but becomes unsteady towards the higher end of the regime. When the flow becomes unsteady, the experimental results were obtained by averaging the taped flow data. Also, towards the higher end of the regime, there is an additional recirculation region along the upper wall, downstream of the expansion. The studies of our numerical results in this flow regime are mostly concerned with these two recirculation regions.

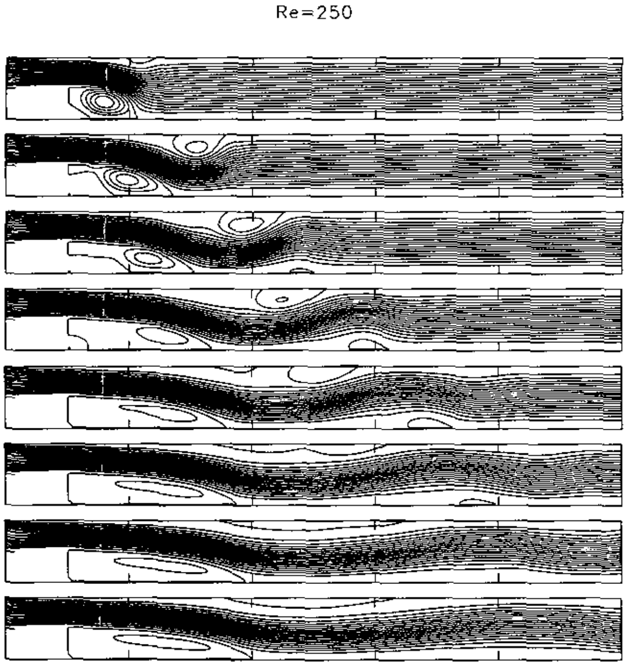

FIG. 7. Instantaneous streamline contours: Re = 250, $h = \frac{1}{32}$, and t = 5, 10, 15, 20, 25, 30, 35, 40.

First, we verified the steadiness of the flow in this regime, with the mesh size 640 × 64. The lowest Reynolds number we used is Re = 25, for which the flow becomes steady within a rather short time. In Fig. 3, we plot the instantaneous streamline contours at t = 5, 10, 15, 20, 25, 30, 35, 40. It is clear that they become indistinguishable after t = 15. To verify this we define

$$\mathbf{u}_\infty(x, y) = \mathbf{u}(x, y, T_\infty) \tag{28}$$

and

$$e(t) = \|\mathbf{u}(t) - \mathbf{u}_\infty\|_{l_2}, \tag{29}$$

then we calculate $e(t)$ to demonstrate the convergence of $\mathbf{u}$ to a steady flow.

In the cases Re = 25, 75, 125, and 250, we chose $T_\infty = 40$. Table I shows the convergence to the steady state with $e(t)$ at different t for different Reynolds numbers. Note that the

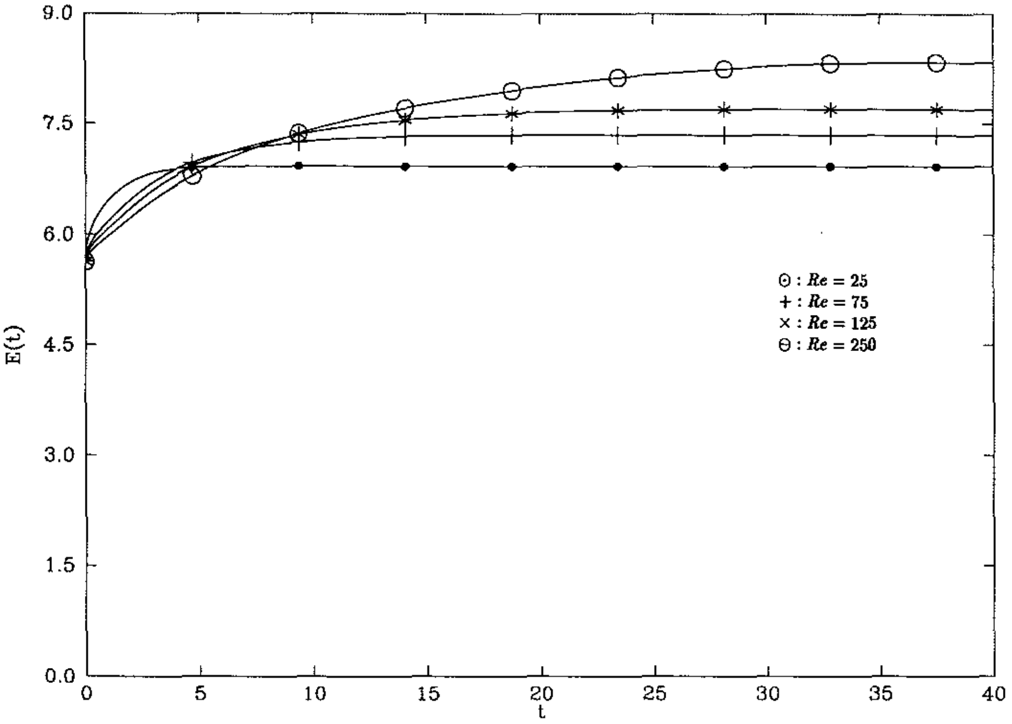

FIG. 9. Kinetic energy as a function of t, at Re = 25, 75, 125, 250.

convergence rate is higher for smaller Reynolds numbers. At Re = 25, the flow becomes exactly steady for $t > 25$ in our output representations. The velocity fields are indistinguishable from each other at least to the sixth decimal place.

In Figs. 4, 5, and 7, we plot the successive instantaneous streamline contours at t = 5, 10, 15, 20, 25, 30, 35, 40, at Re = 75, 125, and 250. Similar results are plotted in Figs. 6 and 8, with a refined grid (960 × 96), at Re = 125 and 250. Obviously it takes longer to reach a steady state at higher Reynolds numbers. An alternative to show this is to plot the total kinetic energy as a function of t (Fig. 9). The rate at which $E_k(t)$ approaches its limit is higher at lower Reynolds numbers than at higher Reynolds numbers.

The most important flow property to calculate and compare in this regime is the reattachment length of the recirculation region. As we see in Fig. 2, at lower Re we have very good agreement between our results and the experimental results. As the Reynolds number increases, we start to lose the agreement. This is probably due to the facts that the flow becomes more and more three-dimensional as Re increases and the inlet length W_I is not large enough. To study the dependence of our results on numerical parameters, we chose the flow at Re = 125 and performed calculations with different numerical parameters, with one parameter change at a time. First we study the mesh size effect by comparing Fig. 5 with Fig. 6. The difference between these two results is rather small and the refined calculation is considered to be fully resolved. Next we increased the inlet length to $W_I = 4$, with the grid size 704 × 64. This would provide longer time for the inlet profile to develop. The new reattachment length from this calculation is $x_R = 5.2936$. Compared with $x_R = 5.07944$ when $W_I = 2$, this is closer to the experiment data in [1]. Therefore, we conclude that the inlet profile does play an important role here. This agrees very well with the conclusion of Ghoniem and Cagnon [12] that the lack of a sufficiently long inlet would cause serious disagreement between a computed solution and the experimental data. This can explain what we observe in Fig. 2 that our curve always lies below the experimental curve. The reason is that we used $W_I = 2$ throughout these calculations and the flows are not fully developed when they reach the step at higher Reynolds numbers.

According to the experimental results, there will be an additional recirculation region along the upper wall when the Reynolds number reaches certain value. At Re = 250, they appear in both Figs. 7 and 8, from results with different mesh sizes. This region is caused by an adverse pressure gradient after the step. To see this, we plot the pressure contours at t = 40, at Re = 25, 75, 125, and 250 in Fig. 10. The contours show changes of the direction of the pressure gradient.

The effect of the recirculation regions can also be seen from the streamwise velocity profiles in the channel. In Fig. 11, we plot the velocity profiles at stations x = 0, 1, 2, 4, 6, 8, 10, 12, 14, and 16, for Re = 25, 75, 125, and 250, at t = 40. At the step ($x = 0$), the profiles are very close to the Poiseuille

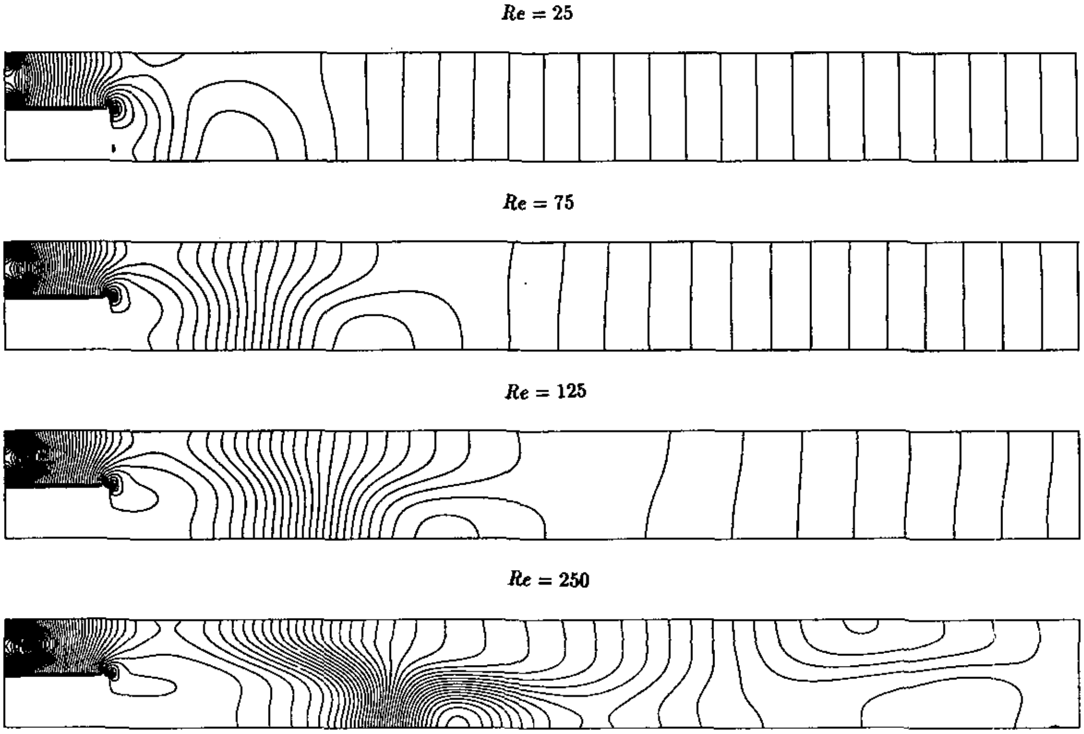

FIG. 10. Pressure contours at t = 40: Re = 25, 75, 125, 250.

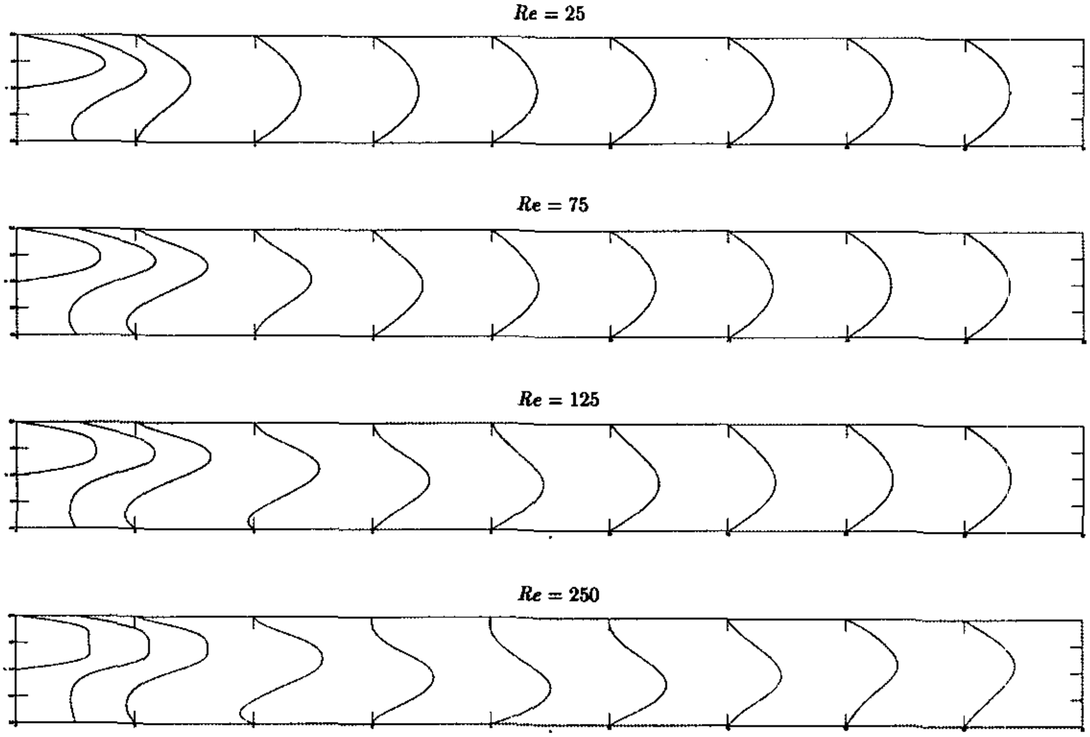

FIG. 11. Streamwise velocity profiles at t = 40: Re = 25, 75, 125, 250, expansion ratio 2 : 1.

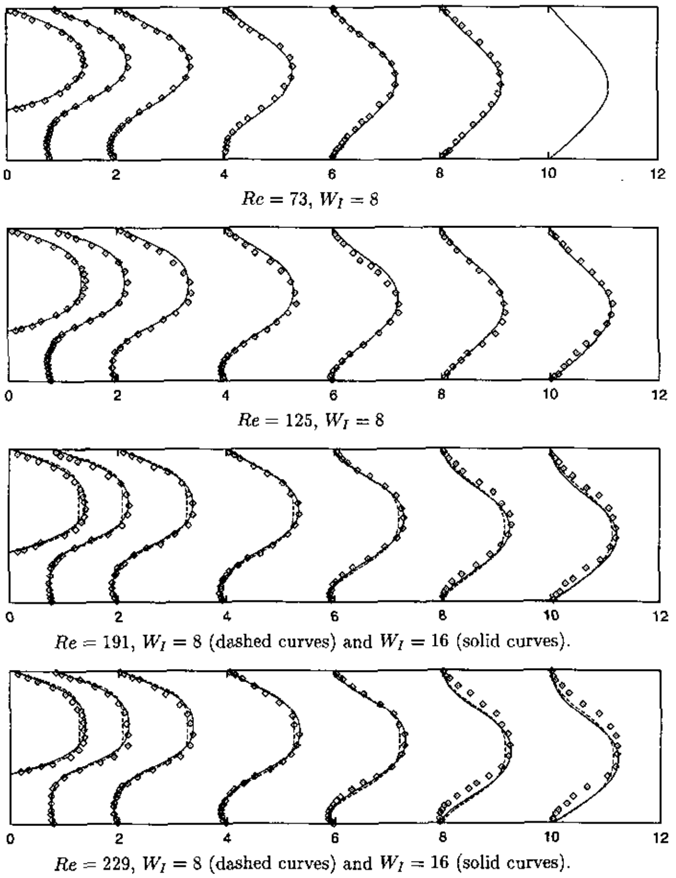

FIG. 12. Comparison between computed and measured velocity profiles at Re = 73, 125, 191, 229. The channel expansion ratio is 3 : 2.

profiles at Re = 25 and 75. At Re = 125 and 250 the presence of the boundary layers shows that the flows are not fully developed. This is caused by the short inlet section W_I we used here. As we will show later, it can be improved with a longer inlet section. At Re = 25, we only note the flow reversal effect at station $x = 1$, and the flow quickly settles to a Poiseuille profile in the downstream direction. This indicates that the effect of the only recirculation region is rather local and restricted. At Re = 75 and 125, we observe the growth of the recirculation regions, and the discrepancy between the computed profiles and the Poiseuille profile is more apparent. In the last plot (Re = 250), we can even detect a tendency of flow reversal along the upper wall (around $x = 8$), which corresponds to a very weak recirculation region (Figs. 7 and 8).

To compare the velocity profiles with the experimental work [8] and numerical work [12], we performed a sequence of calculations with the expansion ratio 3 : 2. The computed profiles at $t = 40$ and the experimental data are plotted in Fig. 12. The solid curves are for the computed solutions and the dots are the experimental results of Denham and Patrick [8]. In these calculations we chose the mesh size $h = \frac{1}{32}$, $W_\mathrm{E} = 18$. We have studied the effect of inlet length on the profiles. First, at Re = 73 and 125, we used $W_\mathrm{I} = 8$ and the profiles at the step seem to be reasonably well developed. The agreement between the computed solution and the experimental data is excellent. When we increased the Reynolds number to Re = 191, $W_\mathrm{I} = 8$ is

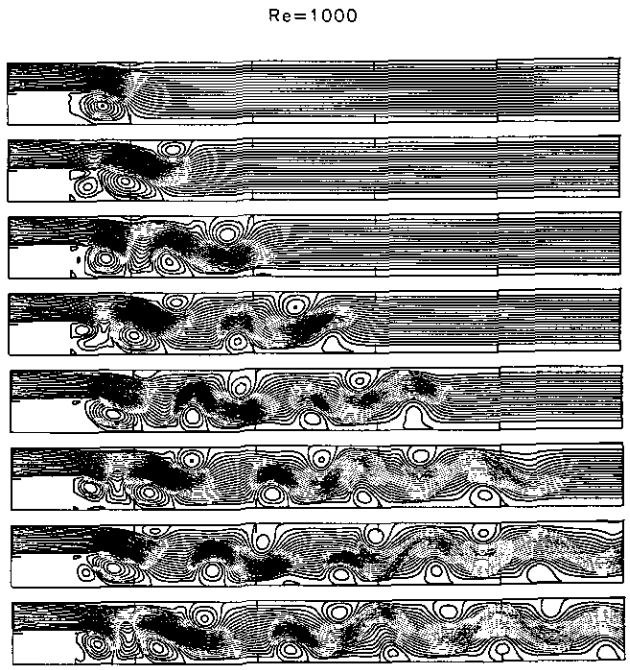

FIG. 13. Instantaneous streamline contours: Re = 1000, $h = \frac{1}{32}$, and t = 5, 10, 15, 20, 25, 30, 35, 40.

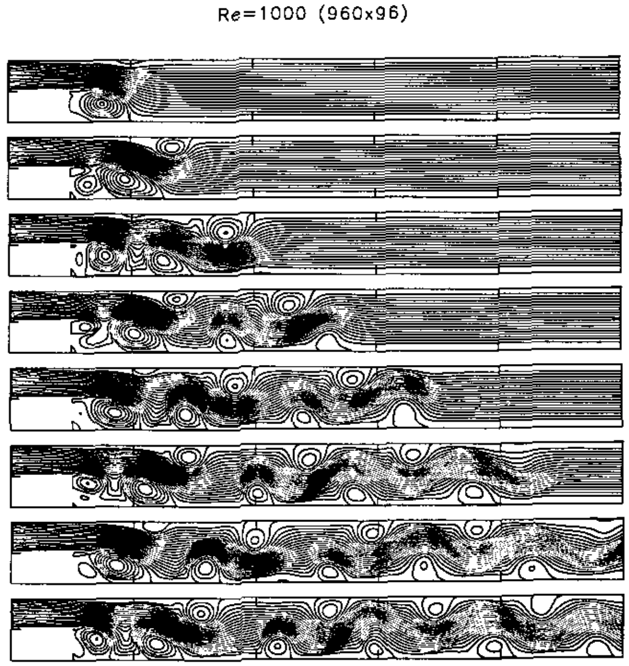

FIG. 14. Instantaneous streamline contours: Re = 1000, $h = \frac{1}{48}$, and t = 5, 10, 15, 20, 25, 30, 35, 40.

not large enough for the flow to be fully developed. In the cases Re = 191 and 229, we plot the computed solutions for both $W_I = 8$ and $W_I = 16$ and the experimental data. The dashed curves are for $W_I = 8$ and the solid curves are for $W_I = 16$. We can see that the first profile at the step with $W_I = 8$ is rather flat, indicating an underdeveloped flow, and the agreement with experimental data is poor. When we increased W_I to 16, the profile at the step is much closer to the Poiseuille profile and the agreement with the experimental data is much improved. As we move downstream, we seem to lose some agreements. This is probably due to the cutoff of our numerical domain and the outflow boundary conditions we imposed. Interestingly enough, for the cases identified in [12], where noticeable discrepancy between their solutions and the experimental data was found, similar disagreement with experimental data also appears in our solution. In the first case ($4 \leq x \leq 8$ at Re = 125), it was suggested in [12] that the accuracy of the experimental measurements was questionable. Our profiles seem to be closer to those in [12]. In the second case ($x \geq 8$ at Re = 229), it is probably that the reattachment length is so large that the channel length $W_E = 18$ is not sufficient. Ghoniem and Cagnon suggested that the existence of a secondary three-dimensional flow was the reason. Again, our profiles deviate from the experimental data in the same way as those in [12]. It should be pointed out that the profiles in this work were generated by the instantaneous velocity fields at $t = 40$, while those in [12] were generated by averaging the flow over a period of time.

3.2. *Transitional and Posttransitional Regimes*

The loss of the steadiness of the flow when the Reynolds number reaches certain value signals the arrival of the transitional regime, where the flow is very unstable after the step. This is also shown by a decrease in the *mean* reattachment length x_R of the main recirculation region with an increase in Reynolds number. The critical Reynolds number where x_R starts to decrease is used to divide the laminar and transitional regimes. From Fig. 2 we note that this particular Reynolds number in our results is slightly lower than that of the experiments. Again, this can be attributed to the three-dimensional nature of the experiments and the insufficient inlet channel length W_I used in our numerical calculations. According to Armaly *et al.* [1], development of longitudinal vortices in this regime is especially strong and it destroys the two-dimensional characters of the flow. When the Reynolds number is further increased, the flow becomes turbulent and it is marked by a mean reattachment length almost independent of the Reynolds number. In both regimes, there is a distinctive vortex shedding mechanism. The main eddy after the step first grows by fluid entrainment; then it splits into two eddies. The new eddy is substantially smaller than the original one and is shed downstream with the flow. The process repeats itself, resulting in a structure with a nearly periodic array of eddies along the lower and upper walls. Even in a sufficiently long time-averaged flow field, there is strong evidence that the additional recirculation regions exist. The averaged flows also show a recirculation region along the upper

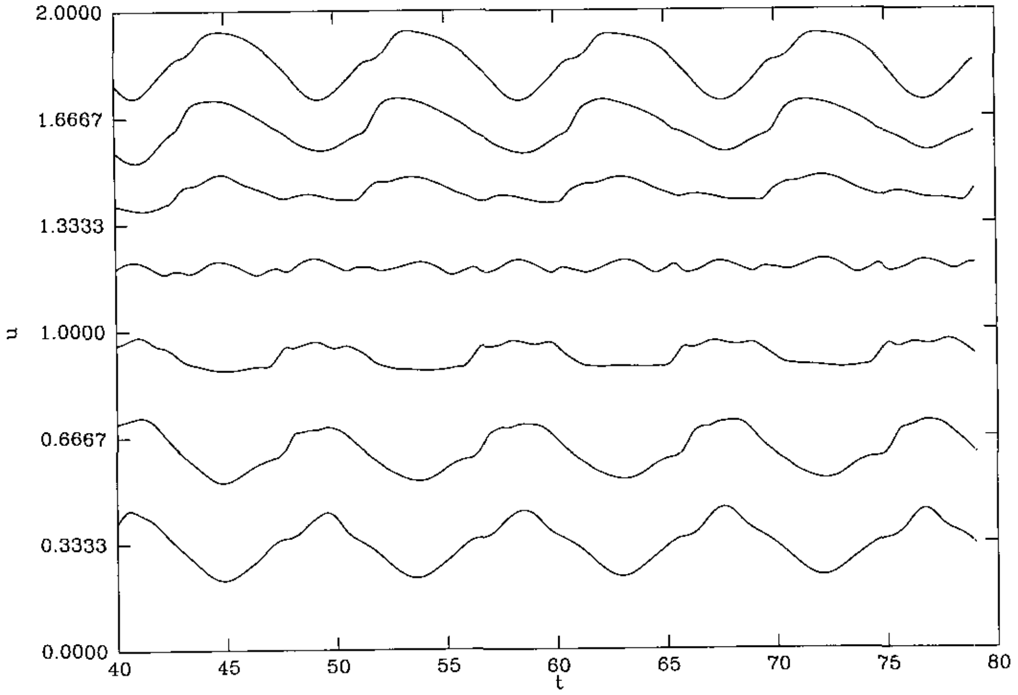

FIG. 15. Streamwise velocity fluctuations in time at points along $x = 16$; Re = 1000.

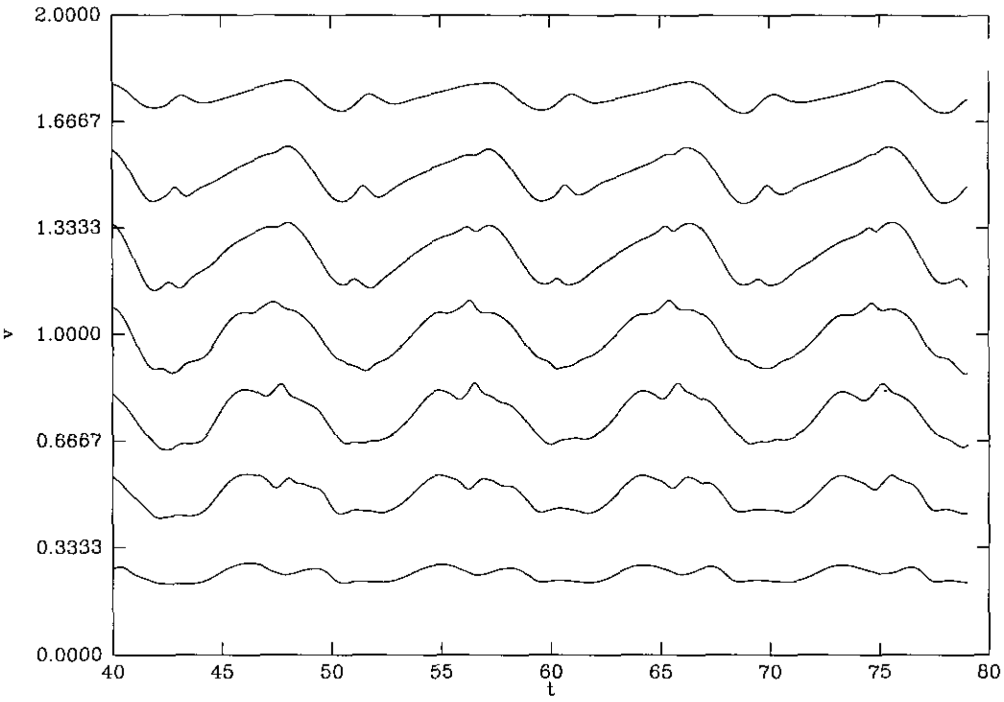

FIG. 16. Cross-stream velocity fluctuations in time at points along $x = 16$; Re = 1000.

wall and it is positioned between two recirculation regions along the lower wall.

In two-dimensional numerical calculations, we do not expect to simulate the fully turbulent flows observed in the experiments for the reasons mentioned in previous sections. For our calculations in the corresponding regime, we should call the regime "post transitional." In Figs. 13 and 14 we show the successive instantaneous streamline contours at t = 5, 10, 15, 20, 25, 30, 35, 40, at Re = 1000, well into the transitional regime, with two grids 640 × 64 and 960 × 96. The periodic array of eddies is well in agreement with results from the experiments and the random vortex method. We also note that the eddies along the upper wall have positive vorticity, while the eddies along the lower wall have negative vorticity. The coherent structure is such that each eddy is positioned in between two corresponding eddies along the opposite wall. In Figs. 15 and 16, we show the velocity fluctuations at a collection of fixed points along the station $x = 16$, where the relative position of a curve corresponds to the position of the point being observed along the line. The periodic structure is obvious and we can see the phase difference for points near the lower and upper walls, which verifies the coherent structure we explained above. The ups and downs indicate the passing of the eddies with a particular frequency which is related to the vortex shedding at the step. We observed in our calculations that the eddies move with a speed approximately equal to $0.37V$, where V is the average inlet velocity. In [16], Sethian and Ghoniem calculated this speed to be close to $\frac{1}{3}V$. It is very important to note that in our calculations this speed is independent of the Reynolds number in this regime.

To obtain more quantitative properties of the flow, we averaged the flow in the following way. We note that around t = 40, the first eddy is about to exit our computational domain. This time was defined as the beginning of our time window for averaging. The length of the time window is chosen to be an integer multiple of the time period required for the second eddy to exit. In this problem, we have found that the time period defined above is approximately 5.5 time units, and we

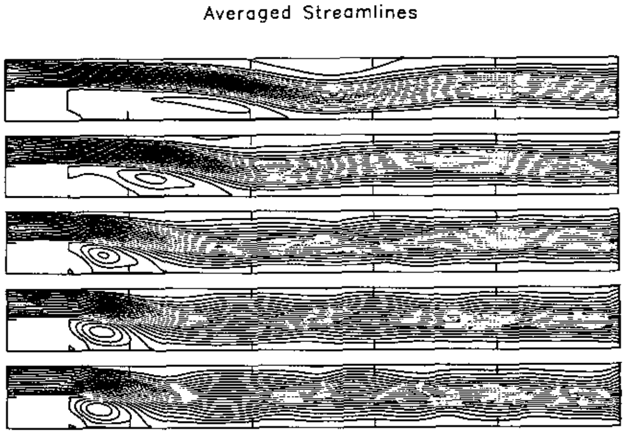

FIG. 17. Streamline contours averaged over time at Re = 500, 750, 1000, 2500, 5000.

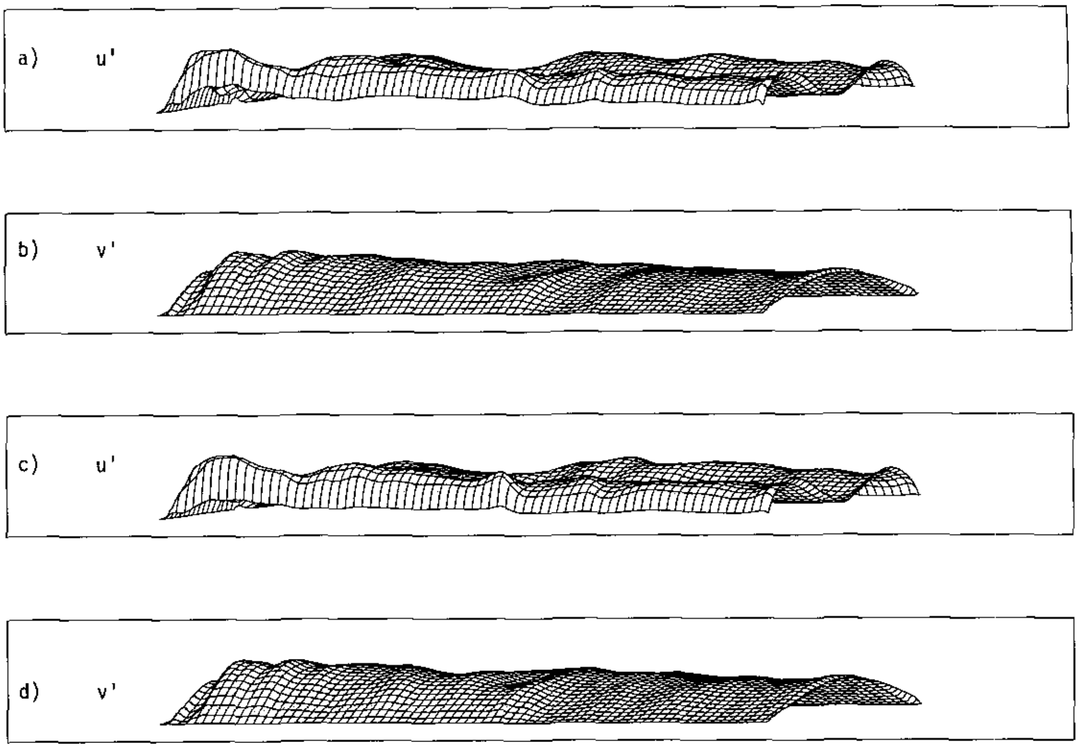

FIG. 18. Comparison of distributions of velocity fluctuations with different grids at Re = 1000: (a) and (b) u, v fluctuations for $h = \frac{1}{32}$; (c) and (d) u, v fluctuations for $h = \frac{1}{48}$. Maximal and average values are shown in Table II.

therefore used a time window [40, 78.75]. All of our averaged quantities are generated using this time window. This includes the results of the mean reattachment length for Re ≥ 500 shown in Fig. 2. In Fig. 17 we plot the averaged streamline contours at Re = 500, 750, 1000, 2500, and 5000. The recirculation structure observed in [1], which includes a primary recirculation region, a secondary region after the primary one, and another one along the upper wall, is verified in these contours. In our plots the secondary regions are so weak in strength that we can barely detect them at really high Reynolds numbers. At relatively low Reynolds number Re = 500, we note a decrease in the reattachment length x_R. After Re = 1000, x_R does not change that much. As the Reynolds number increases, the recirculation region along the upper wall moves upstream and becomes weaker. This behavior of the averaged streamlines agrees very well with the similar behavior of solutions from the random vortex method.

The major question of the calculations in these two regimes is to justify the numerical method for a physically unstable flow. To give some evidence that we have captured some characteristics of the instability associated with solutions of the two-dimensional Navier–Stokes equations in this geometry, we proceeded with the following convergence study. We chose a fixed Reynolds number Re = 1000 and started with a 640 × 64 grid, then we refined it to a 960 × 96 grid. In the transitional and posttransitional regimes, the pointwise convergence does not make any sense. So we turn to the convergence of the averaged velocity fluctuation. The averaged velocity fluctuation $\mathbf{u}'$ is defined through its components u' and v' by

$$u'^2 = \overline{(u - \overline{u})^2} = \frac{1}{T}\int_{t_1}^{t_1+T} (u - \overline{u})^2 \, dt, \tag{30}$$

and a similar formula for v', where $\overline{\mathbf{u}} = (\overline{u}, \overline{v})$ is the average of $\mathbf{u}$ over the time window $[t_1, t_1 + T]$ and it is given by

$$\overline{\mathbf{u}} = \frac{1}{T}\int_{t_1}^{t_1+T} \mathbf{u} \, dt. \tag{31}$$

In our calculations, we chose $t_1 = 40$ and $T = 38.75$. In Fig. 18, we plot the velocity fluctuations as functions of (x, y) for both components u' and v', in the domain $[0, 18] \times [0, 2]$, and we compare the results between two different grids. It is apparent that the distributions of the fluctuation are very similar in these two different calculations. For u', the maximum is in the left lower corner region, which corresponds to the major recirculation region. The wavy distribution along the walls may correspond to the passing of the eddies. It is also observed that u' is rather small in the center of the channel, which indicates

TABLE II

Velocity Fluctuation

h	$\|u'\|_{l_\infty}$	$\|v'\|_{l_\infty}$	$\|u'\|_{l_1}$	$\|v'\|_{l_1}$
1/32	0.544061	0.514668	0.220915	0.224002
1/48	0.545859	0.508991	0.218105	0.223004

that u is relatively stable there. The fluctuation u' on the lower edge of the plot (the upper edge cannot be seen in this plot) is not zero, which seems to contradict what would be expected from the physical boundary condition. The reason is that our velocity is defined at the center of a cell, so the edge points in the plot are not really on the physical boundary. At Re = 1000, the transition of the tangential component of the velocity in the boundary layer is very sudden, so there could be some substantial tangential velocity at these edge points. The step boundary ($x = 0$, $0 \leq y \leq 1$) can be seen in these plots (the left lower edges) and the fluctuation there is quite small. For v', it is very close to zero near the boundary. This agrees with the boundary layer analysis. The maximum occurs after the channel expansion, indicating a strong fluctuation in the pressure gradient there. Compared to u', it is quite large in the center of the channel. In Table II, the maximal and average values of u' and v' are given. Considering that the average velocity u is 0.5, the average fluctuation shown in the table is quite strong. The significance of this comparison between two calculations is that we can contribute almost all of the instability in our numerical solutions to the unstable nature of the two-dimensional Navier–Stokes equations at high Reynolds numbers.

4. SUMMARY

We have used the second-order projection method to study the two-dimensional flow in a long channel with a backward-facing step, in all of three flow regimes defined by the Reynolds number. In the laminar regime, excellent agreement between our numerical results and experimental data is obtained. We noted the importance of the inlet channel length in these calculations. With the second-order nature of the method, we are able to resolve the flow with a 640 × 64 grid. Further refining of the grid does not make noticeable changes in the flow properties in which we are interested. In the transitional and posttransitional regimes, the lack of any two-dimensional experimental data for comparison makes it difficult to reach a definite conclusion. However, some characteristics of the flow observed in three-dimensional experiments were verified in our numerical results. Again, the basic properties are not substantially changed with refined calculations. At extremely high Reynolds numbers, such as Re = 5000, the numerical viscosity may contaminate the physical viscosity to such an extent that calculations with further increased Reynolds numbers are questionable. Direct comparisons were made with results from the random vortex method and experiments in the same settings, and agreement was found both in the qualitative characteristics of the flow and quantities such as the mean reattachment length and streamwise velocity profiles. A major issue in this problem is that we want to isolate the physical instability of the flow from any numerical instability caused by a numerical method. Here we have succeeded in generating a sequence of calculations with different mesh sites similar velocity fluctuations in time. This provides us with some evidence that the instability we observed in the numerical results is indeed related to the original differential equations.

Eventually, a totally convincing numerical calculation would be a three-dimensional calculation. The projection method is capable of being extended naturally to three dimensions. Therefore, the next step of the investigation of the step problem should be a fully three-dimensional calculation with the second-order projection method.

ACKNOWLEDGMENTS

The author is grateful to Phillip Colella for important suggestions and to Alexandre Chorin, Aaron Fogelson, and James Sethian for helpful discussions. The comments and suggestions of a reviewer are also gratefully acknowledged. The author thanks Nelson Beebe for his help with the figures. Calculations were performed at the Lawrence Livermore National Laboratory and at the Utah Supercomputing Institute.

REFERENCES

1. B. Armaly, F. Durst, J. Pereira, and B. Schönung, *J. Fluid Mech.* **127,** 473 (1983).
2. W. T. Ashurst, in *2nd Symposium on Turbulent Shear Flows, Imperial College, London, July 1979* (unpublished).
3. J. Bell, P. Colella, and H. Glaz, *J. Comput. Phys.* **85,** 257 (1989).
4. J. B. Bell and D. L. Marcus, *J. Comput. Phys.* **101,** 334 (1992).
5. A. J. Chorin, *Math. Comput.* **22,** 745 (1968).
6. A. J. Chorin, *Math. Comput.* **23,** 341 (1969).
7. P. Colella, *J. Comput. Phys.* **87,** 171 (1990).
8. M. K. Denham and M. A. Patrick, *Trans. Inst. Chem. Eng.* **52,** 361 (1974).
9. F. Durst and C. Tropea, in *Proc. Turbulent Shear Flow 3 Symp., Davis, September 1981* (unpublished).
10. A. F. Ghoniem, A. J. Chorin, and A. K. Oppenheim, *Philos. Trans. R. Soc. London A* **304,** 303 (1982).
11. A. F. Ghoniem and J. Sethian, in *AIAA 23rd Aerospace Sciences Meeting, Reno, Nevada, January 1985;* AIAA-85-0146 (unpublished).
12. A. F. Ghoniem and Y. Cagnon, *J. Comput. Phys.* **68,** 346 (1987).
13. E. O. Macagno and T. K. Hung, *J. Fluid Mech.* **28,** 43 (1967).
14. H. Najm and A. F. Ghoniem, *AIAA J.* **29**(6), 911 (1991).
15. J. Periaux, O. Pironneau, and F. Thomasset, "Computational Results of the Back Step Flow Workshop," in *Fifth International GAMM Conference on Numerical Methods in Fluid Mechanics* (Springer-Verlag, New York/Berlin, 1983).
16. J. A. Sethian and A. F. Ghoniem, *J. Comput. Phys.* **74,** 283 (1988).
17. A. B. Stephens, J. B. Bell, J. M. Solomon, and L. B. Hackerman, *J. Comput. Phys.* **53,** 152 (1984).